ACS Catalysis

Research Article

pubs.acs.org/acscatalysis

Surface-Structure Sensitivity of CeO_2 Nanocrystals in Photocatalysis and Enhancing the Reactivity with Nanogold

Wanying Lei,[†] Tingting Zhang,[†] Lin Gu,[‡] Ping Liu,[§] José A. Rodriguez,[§] Gang Liu,*[,†] and Minghua Liu*[,†]

[†]National Center for Nanoscience and Technology, Beijing 100190, China

[‡]Beijing National Laboratory for Condensed Matter Physics, Institute of Physics, Chinese Academy of Sciences, Beijing 100190, China

[§]Chemistry Department, Brookhaven National Laboratory, Upton, New York 11973, United States

Supporting Information

ABSTRACT: Structure–function correlations are a central theme in heterogeneous (photo)catalysis. In this study, using aberration-corrected scanning transmission electron microscopy (STEM), the atomic surface structures of well-defined one-dimensional (1D) CeO_2 nanorods (NRs) and 3D nanocubes (NCs) are directly visualized at subangstrom resolution. CeO_2 NCs predominantly expose the {100} facet, with {110} and {111} as minor cutoff facets at the respective edges and corners. Notably, the outermost surface layer of the {100} facet is nearly O-terminated. Neither surface relaxations nor reconstructions on {100} are observed, indicating unusual polarity compensation, which is primarily mediated by near-surface oxygen vacancies. In contrast, the surface of CeO_2 NRs is highly stepped, with the enclosed {110} facet exposing Ce cations and O anions on terraces. On the basis of STEM profile-view imaging and electronic structure analysis, the photoreactivity of CeO_2 nanocrystals toward aqueous methyl orange degradation under UV is revealed to be surface-structure-sensitive, following the order: {110} ≫ {100}. The underlying surface-structure sensitivity can be attributed to the variation in low-coordinate surface cerium cations between {110} and {100} facets. To further enhance light absorption, Au nanoparticles (NPs) are deposited on CeO_2 NRs to form Au/CeO_2 plasmonic nanocomposites, which dramatically promotes the photoreactivity that is Au particle size- and excitation light wavelength-dependent. The mechanisms responsible for the enhancement of photocatalytic activity are discussed, highlighting the crucial role of photoexcited charge carrier transfer.

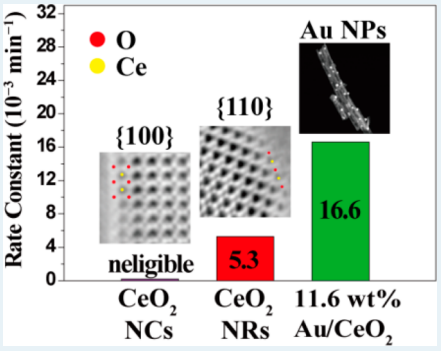

KEYWORDS: *surface structure, CeO_2, aberration-corrected STEM, photocatalysis, surface plasmon resonance, nanogold*

INTRODUCTION

Heterogeneous photocatalysis has received growing attention in recent years and become a technologically emerging approach to the sustainable development of environment and energy, such as organic pollutant removal from wastewater streams,[1,2] organic synthesis,[3] and water splitting for hydrogen generation.[4,5] It is generally accepted that structure–function relationships are a central theme in heterogeneous catalysis; that is, the catalytic property of a given catalyst is determined by its crystallographic facets and surface terminations.[6] Thus, controlling the size, shape, and dimensionality of catalysts is crucial for optimizing the catalytic reactivity,[7,8] selectivity,[9] and stability.[9] For example, one-dimensional (1D) anisotropic nanostructures often present a high surface area and a great number of surface active sites compared with their bulk counterparts.[10] Further, the photoexcited charge separation and transportation could be tuned in 1D nanostructures via quantum confinement.[11] Until now, the vast majority of photocatalytic studies have been focused on titanium dioxide (TiO_2);[12−14] far less information is available about other materials. To this end, the quest of a diverse set of high-performance photocatalysts is beneficial to both fundamental and applied heterogeneous photocatalysis.

Owing to the high oxygen storage capacity and unique redox properties, fluorite-structured ceria (CeO_2) has been extensively studied in a number of technologically relevant processes, such as automobile three-way catalysis, water–gas shift reactions, and gas sensors.[15−17] Previous studies have reported that the low-index {100} and {110} crystallographic facets of CeO_2 are more reactive than the {111} facet, in part consistent with the surface energy order {100} > {110} > {111}.[18,19] In particular, the {100} facet of CeO_2 is an inherent polar surface owing to the alternating layers of cations and anions in the bulk structure. Therefore, there exists polarization (i.e., a finite dipole moment) along the surface normal. In a simplified model, surface reconstructions occur. In this case, about half of terminated oxygen anions are removed to compensate the polarity.[20] However, the exact surface structures of nanoscaled

Received: March 23, 2015
Revised: June 5, 2015
Published: June 5, 2015

DOI: 10.1021/acscatal.5b00620
ACS Catal. 2015, 5, 4385−4393

CeO_2 still remain unclear. Unlike surface chemistry and thermal heterogeneous catalysis, there are only a few reports about CeO_2 in heterogeneous photocatalysis.[1,21] And systematic studies on CeO_2 photocatalysts with well-defined shapes are largely unexplored. In general, only in-depth understanding of well-defined model photocatalysts could provide insights into the structure−function relationships and potentially generate new concepts for directing the rational design of efficient photocatalysts. Thanks to recent progress of aberration-corrected transmission electron microscopy (TEM),[22] in which it is possible to reveal the outermost surface layer by profile-view imaging and correlate the structure−photoreactivity relationships at atomic scale. In the view of utilizing the full solar spectrum in photocatalytic processes, bandgap engineering,[23] doping,[1] and loading noble metal nanoparticles (NPs)[24] have been developed to prepare a variety of visible-light-responsive materials. In particular, the integration of plasmonic metals such as gold (Au) NPs onto wide-bandgap semiconductors such as CeO_2 is the most efficient and facile route to enhance photocatalytic performance via unique surface plasmon resonance (SPR) that originates from Au NPs.[25]

In this study, we directly visualized the atomic surface structure of 1D CeO_2 nanorods (NRs) and 3D nanocubes (NCs) by aberration-corrected scanning transmission electron microscopy (STEM), in which both light oxygen and heavier cerium can be directly determined at subangstrom resolution, and the understanding of imaging contrast is straightforward. We uncover unusual polarity compensation primarily mediated by near-surface oxygen vacancies. Further, the photoreactivity of the as-prepared CeO_2 NRs and NCs was examined toward photodegradation of methyl orange (MO) in water, a model reaction in the removal of organic dye pollutants from wastewater. We reveal that the origin of structure-sensitive photoreactivity can be attributed to the variation in low-coordinate surface cerium cations between {100} and {110} facets. Additionally, loading Au NPs onto CeO_2 NRs to form plasmonic nanocomposites further enhances the photoreactivity.

EXPERIMENTAL SECTION

Preparation of CeO_2 Nanocrystals. CeO_2 NRs and NCs were hydrothermally prepared.[26] Briefly, 4 mmol of $Ce(NO_3)\cdot 6H_2O$ (99.5% purity, Alfa Aesar) was dissolved in 10 mL Milli-Q (18 MΩ·cm, Millipore) water and then added into a 6 M NaOH (Alfa Aesar) solution. The mixture was vigorously stirred under ambient temperature for 30 min. The white slurry was then transferred into an autoclave (100 mL) and maintained at 120 °C, 24 h for NRs, and 180 °C, 48 h for NCs to get well-defined samples. Next, the fresh precipitates were collected by centrifugation, washed with Milli-Q water and ethanol, then dried at 60 °C overnight and finally calcined at 550 °C for 2 h in air with a heating ramp of 4 °C·min^{-1}.

Preparation of Au/CeO_2 Plasmonic Nanocomposites. Gold NPs were deposited onto CeO_2 NRs through a deposition-precipitation method. Briefly, 0.2 g of CeO_2 NRs was dispersed in 100 mL of Milli-Q water, then the suspension was heated to 80 °C. A certain amount of hydrogen tetrachloroaurate(III) trihydrate ($HAuCl_4\cdot 3H_2O$, 99.99% purity, Alfa Aesar) solution (10 g·L^{-1}) was added stepwise to the suspension. A 0.2 M NaOH aqueous solution was gradually added until the pH value was up to 9.0. The mixture was vigorously stirred for 2 h. The sample was isolated by centrifugation and washed with hot Milli-Q water to remove chloride anions, then dried overnight. Finally, the as-obtained catalysts were calcined at 200 °C for 2 h in air. The actual Au weight was determined by inductively coupled plasma atomic emission spectrometer (ICP-AES) in an Optima 4300 DV spectrometer (PerkinElmer).

Characterization. Powder X-ray diffraction (XRD) patterns were obtained on a Shimadzu X-ray diffractometer (XRD-6000) with Cu Kα radiation (λ = 0.154178, 50 kV, 300 mA) at a scanning rate of 4° min^{-1} in the 2θ range of 10−85°. The Raman spectra were collected on a Renishaw Micro-Raman spectroscopy system (Renishaw in via plus) with a 514 nm laser. The Brunauer−Emmett−Teller (BET) specific surface area was measured through nitrogen adsorption using a Micromeritics ASAP 2000 apparatus. Diffuse reflectance ultraviolet and visible spectra in the range of 200−800 nm were obtained using a PerkinElmer Lambda 950 UV−vis spectrometer. Fine MgO powders were used as a standard. X-ray photoelectron spectroscopy (XPS) data were obtained by an ESCALab 250 electron spectrometer from Thermo Scientific Corporation. Monochromatic 150 W Al Kα radiation was utilized, and low-energy electrons were used for charge compensation. All binding energies (BE) were referenced to the adventitious C 1s line at 284.8 eV. Commercial software (Avantage) was used for curve-fitting. The XPS spectra were modeled by Voigt peak profiles after subtracting a Shirley-type background. Further, the %Lorentzian−Gaussian for the Au 4f spectra was fixed at 20%. The O *K*-edge X-ray absorption near-edge structure (XANES) spectra were taken at the Photoelectron Spectroscopy Station of the Beijing Synchrotron Radiation Facility of the Institute of High Energy Physics, Chinese Academy of Science. Photoemission experiments were carried out in an ultrahigh vacuum chamber with a base pressure of ~8×10^{-10} Torr, and the energy resolution was 0.5 eV in the total electron yield detection mode. All spectra were normalized to the incident photon flux, and the energy calibration was performed by an Au foil. Transmission electron microscopy (TEM) was conducted by a 200 kV Tecnai G^2 F20 U-TWIN microscope. High-angle annular dark-field (HAADF) and annular bright-field (ABF)-STEM imaging were performed using a JEOL JEM ARM 200F (Tokyo, Japan) TEM equipped with a CEOS (Heidelberg, Germany) probe aberration correctors. The original images were Fourier-filtered to remove noise.

Photocatalysis Evaluation. The photocatalytic activities of the as-prepared samples were evaluated toward photodegradation of MO in water. Prior to irradiation, 25 mg of photocatalyst was dispersed into a 50 mL MO (4×10^{-4} M) aqueous solution in a 150 mL beaker. Subsequently, the solution was sonicated for 10 min and magnetically stirred in the dark for 60 min to ensure the complete adsorption−desorption equilibrium of MO on the surface of photocatalysts. A 300 W xenon lamp was used as the excitation source positioned ~9 cm above the beaker. The light intensity in the center of the beaker was measured to be ~300 mW·cm^{-2} using a Newport optical power/energy meter (842-PE). During the illumination, the reaction temperature was maintained at room temperature. For the UV experiment, a UV reference (250 nm < λ < 380 nm) was used. In the case of the visible light experiment, a 420 nm cutoff filter was utilized to allow visible light (λ > 420 nm) to transmit. At certain time intervals, ~3.0 mL of suspension was collected and centrifuged at 15000 rpm for 3 min to remove catalyst powders. The photoreactivity was monitored by measuring the absorbance of the solution at the

DOI: 10.1021/acscatal.5b00620
ACS Catal. 2015, 5, 4385−4393

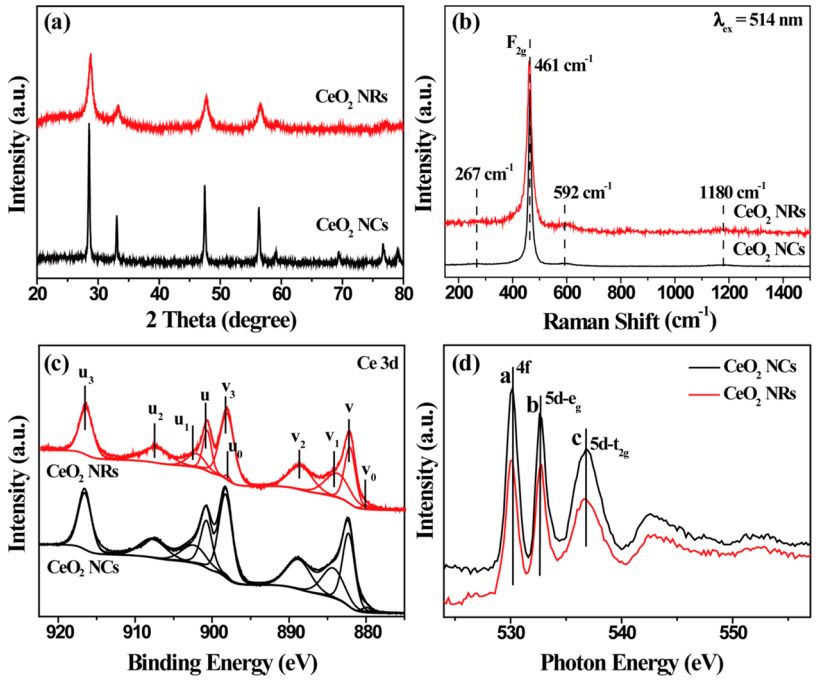

Figure 1. Characterization of CeO_2 NCs and NRs. (a) Powder XRD patterns. (b) Micro-Raman spectra. (c) High-resolution XPS spectra of Ce 3d core-level and (d) O *K*-edge XANES spectra.

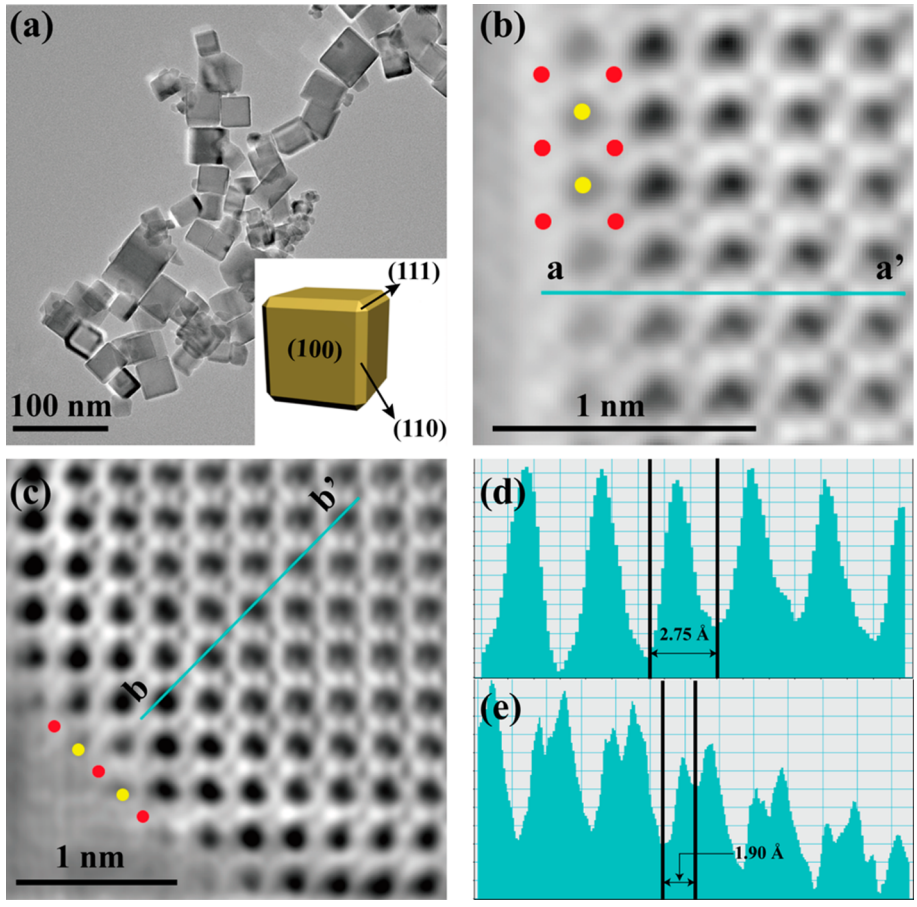

Figure 2. Characterization of CeO_2 NCs by TEM and STEM. (a) Low-magnification TEM image of CeO_2 NCs. Inset: Schematic drawing of CeO_2 NCs. (b) Atomically resolved ABF-STEM image of the {100} facet viewed along the [001] direction. The yellow and red spheres represent Ce and O ions, respectivly. (c) Atomically resolved ABF-STEM image of the {110} facet exposed at the edge of CeO_2 NCs. Corresponding line profiles showing the image intensity as a function of position (d) along a−a′ in image b, and (e) along b−b′ in image c.

DOI: 10.1021/acscatal.5b00620
ACS Catal. 2015, 5, 4385−4393

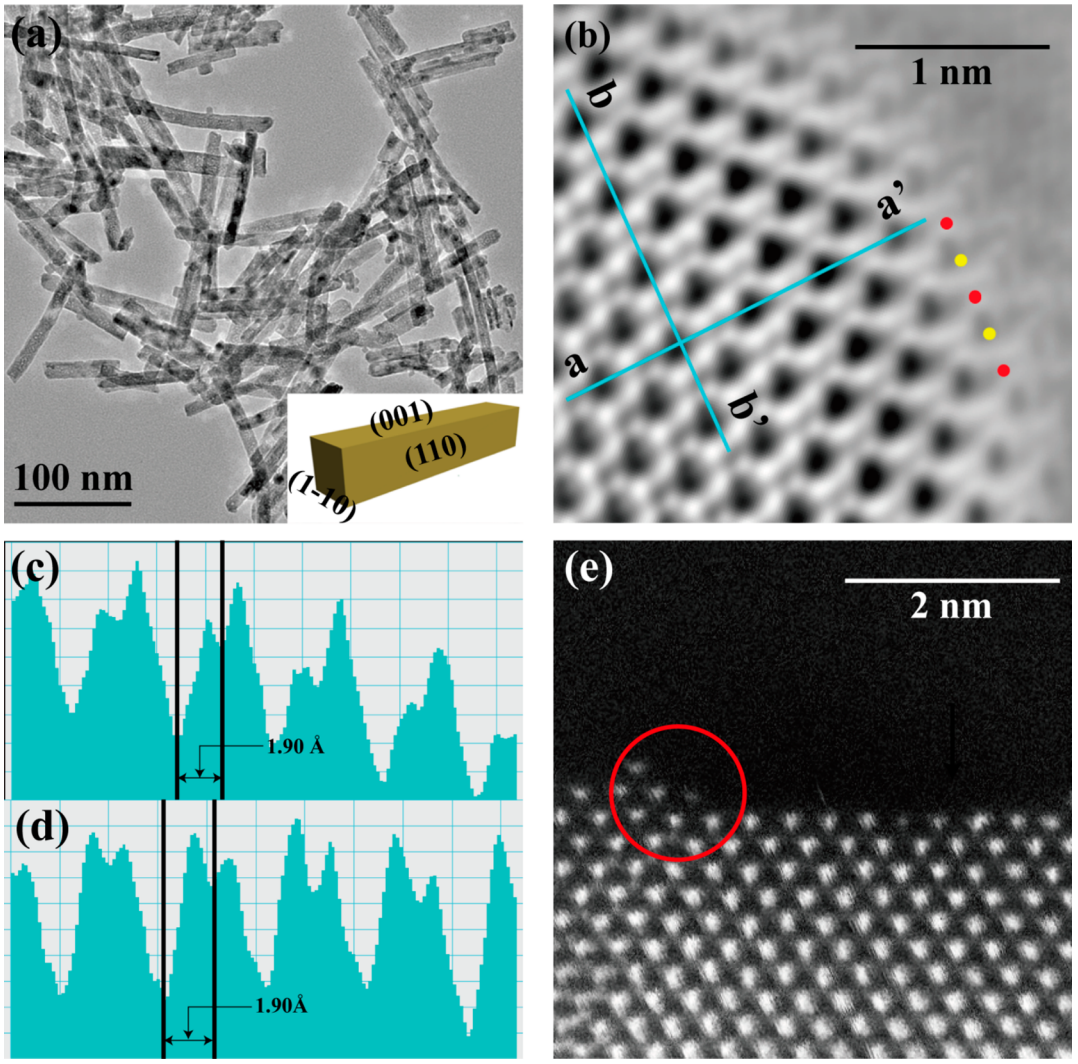

Figure 3. Characterization of CeO_2 NRs by TEM and STEM. (a) Low-magnification TEM image of CeO_2 NRs. Inset: Schematic drawing of CeO_2 NRs. (b) Atomically resolved ABF- STEM image of the {110} facet viewed along the [001] direction. The yellow and red spheres represent Ce and O ions, respectivly. Corresponding line profiles showing the image intensity as a function of position (c) along a–a′ in image b, and (d) along b–b′ in image b. (e) The atomic steps evidenced by HAADF-STEM imaging are highlighted by a red circle.

maximum wavelength of 463 nm (MO) using a PerkinElmer Lambda 950 UV–vis spectrometer.

RESULTS

Sample Characterization. Figure 1a depicts the XRD patterns of the as-prepared pristine CeO_2 NCs and NRs. All diffraction lines can be indexed to the fluorite cubic structure of CeO_2 (JCPDS 43-1002, *Fm*3*m* space group with lattice parameter a = 0.5418 nm). The NCs exhibit sharper XRD peaks than the NRs. The crystallite size as calculated from the Scherrer equation is 9.3 and 28.8 nm for NRs and NCs, respectively. The Raman spectra are displayed in Figure 1b. Under light excitation at 514 nm, a typical band located at 461 cm^{-1} is attributed to the first-order vibrational mode with F_{2g} symmetry in a fluorite cubic structure, that is , the symmetric vibrating mode of the O anions around a Ce cation. The other weaker bands around 267 and 1180 cm^{-1} are assigned to the second-order transverse acoustic (2TA) and longitudinal optical (2LO) modes, respectively. The broad band located at 592 cm^{-1} corresponds to oxygen vacancies.[26] The chemical compositions and oxidation states are probed by XPS. Figure 1c shows high-resolution XPS spectra of Ce 3d core-level with multiple peaks that are decomposed into 10 well-resolved subpeaks by curve-fitting, with u and v referring to Ce $3d_{3/2}$ and Ce $3d_{5/2}$, respectively.[26] In detail, the peaks labeled as v (882.2 eV), v_2 (888.8 eV), v_3 (898.2 eV), u (900.7 eV), u_2 (907.5 eV), and u_3 (916.6 eV) are ascribed to Ce^{4+} ions. Other peaks denoted as v_0, v_1, u_0, and u_1 are characteristics of Ce^{3+} ions. The concentration of Ce^{3+} is estimated to be ~20% for both CeO_2 NCs and NRs. Therefore, the concentration of oxygen vacancies is ~10% in the surface and subsurface region, taking into account that two Ce^{3+} cations are associated with the formation of one oxygen.[27] Figure S1a (Supporting Information) illustrates the valence band (VB) spectra of CeO_2 nanocrystals. The band maxima of NCs and NRs are located at 1.96 and 2.28 eV, and the bandwidth (~6.01 eV) is almost identical between NCs and NRs. The relatively weak peak near the Fermi level is ascribed to Ce^{3+} species.[28] The O 1s core-level spectra are displayed in Figure S1b (Supporting Information). The peak at 529.4 eV is ascribed to lattice oxygen and the peak located at higher binding energy corresponds to the oxygen species of water. It is well-known

DOI: 10.1021/acscatal.5b00620
ACS Catal. 2015, 5, 4385–4393

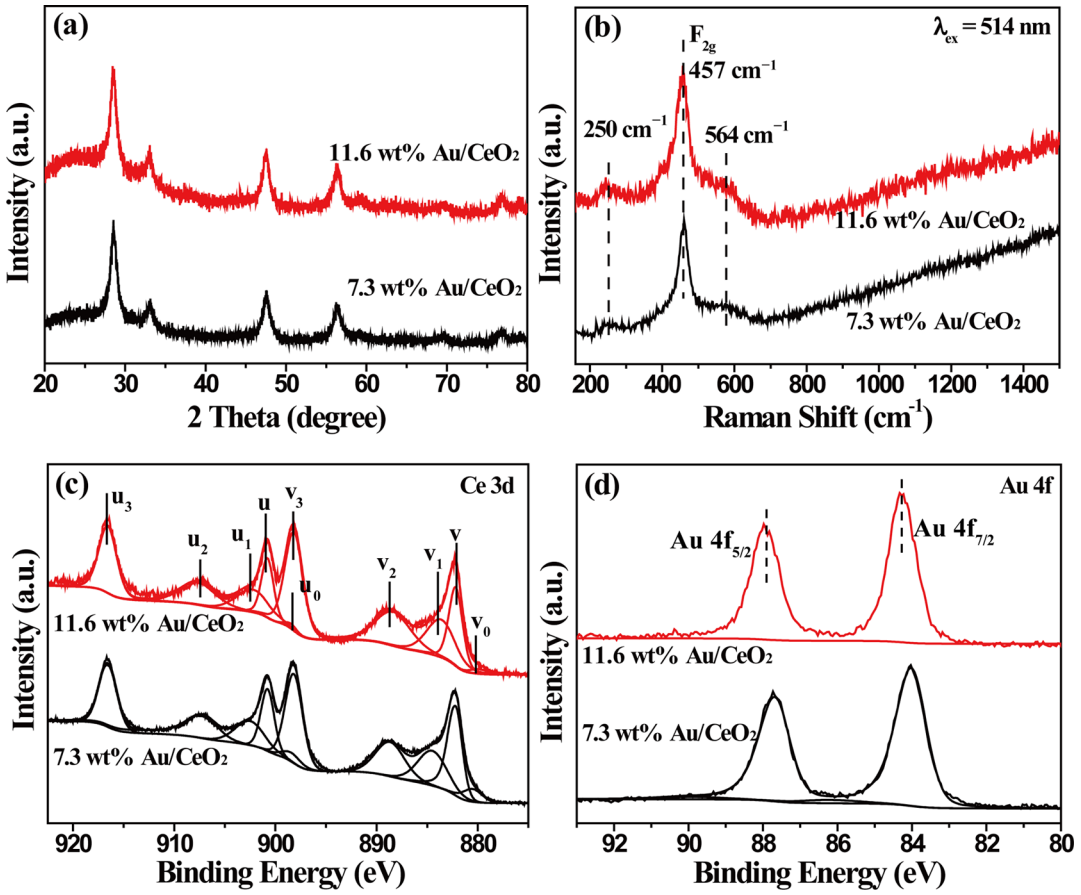

Figure 4. Characterization of Au/CeO_2 nanocomposites. (a) Powder XRD patterns. (b) Micro-Raman spectra. High-resolution XPS spectra of (c) Ce 3d core level and (d) Au 4f core level.

that *K*-edge features of transition metal oxides are very sensitive to the chemical environment around the X-ray absorbing atoms.[28] Figure 1d shows O *K*-edge XANES spectra of CeO_2 NRs and NCs. Peak a centered at 530.1 eV is attributed to the electronic transition from the O 1s core level into the empty Ce 4f level. Both peaks b and c observed at 532.6 and 536.8 eV, respectively, are related to the O 1s → Ce 5d electronic transition, and 4.2 eV between these two peaks reflects the splitting of Ce 5d orbits into the levels with e_g and t_{2g} symmetries. The relative intensity ratio (a/b) between peaks a and b is slightly increased from CeO_2 NRs to NCs, suggesting the minor difference in electronic structure between CeO_2 NRs and NCs.[28] The BET specific surface area of CeO_2 NCs and NRs is 32.8 and 62.5 $m^2 \cdot g^{-1}$, respectively.

Figure 2a shows a typical TEM image of CeO_2 NCs at low magnification. The size of well-defined CeO_2 NCs is in the range of 15−40 nm. To elucidate the surface structures of CeO_2 nanocrystals at the atomic level, we utilize aberration-corrected STEM. Generally, aberration-corrected STEM imaging contrast strongly depends on the atomic number (Z) of elements: the contrast of ABF imaging displays a $Z^{1/3}$ dependency that is different from $Z^{1.7}$ dependency for HAADF imaging. Light elements such as oxygen that are barely visualized in HAADF imaging can be directly observed through ABF imaging.[29,30] In the present study, we combine HAADF- and ABF-STEM profile-view imaging to characterize CeO_2 surface structures. A representative ABF image of a cube viewed along the [001] direction is illustrated in Figure 2b. The black and gray spots correspond to Ce and O ions, respectively.[30] The interatomic distance obtained by line profile along a−a′ is measured to be 2.75 Å (Figure 2d), in good agreement with (100) spacing of CeO_2. The outermost surface layer of the {100} facet is revealed to be O-terminated. No surface reconstructions are observed. Moreover, the distance between the O columns in the outermost layer and the Ce columns in the subsurface layer is measured to be 1.37 Å, which is consistent with the distance in the bulk. Therefore, no surface relaxations occur as well. Additionally, atomic steps with one layer height are occasionally observed and still terminated with O, as shown in Figure S2a (Supporting Information). In contrast, the truncations at the edges of CeO_2 NCs present a CeO termination as displayed in Figure 2c. The interatomic distance along b−b′ is 1.90 Å (Figure 2e), in accordance with (110) spacing. The {111} facet originates from the truncations between two adjacent {100} facets. On the basis of our direct atomic-level observations, a schematic drawing of the geometrical shape for CeO_2 NCs is illustrated in the inset of Figure 2a. CeO_2 NCs predominantly expose six {100} facets, with twelve {110} facets at the edges and eight {111} facets at the corners.

Figure 3a shows a representative TEM image of elongated CeO_2 NRs. The length and the width are in the range of 30−370 and 7−13 nm, respectively. A close look at one typical rod by ABF imaging viewed along the [001] direction shows that the outermost surface layer is composed of coexisting Ce cations and O anions (Figure 3b). The interatomic distance obtained by line profiles along both a−a′ and b−b′ from Figure 3b is 1.90 Å (Figure 3c and d), consistent with (110) spacing.

DOI: 10.1021/acscatal.5b00620
ACS Catal. 2015, 5, 4385−4393

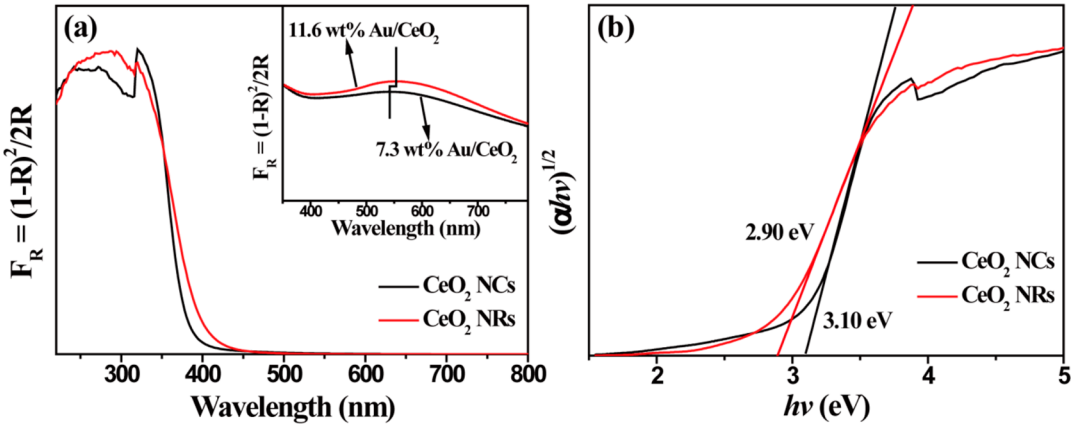

Figure 5. (a) DRUV−vis spectra of the as-prepared CeO_2 nanocrystals and Au/CeO_2 nanocomposites. Inset: surface plasmon bands displayed by Au NPs. (b) Corresponding plots of $(\alpha h\nu)^{1/2}$ versus photon energy ($h\nu$) of CeO_2 nanocrystals.

The surface of CeO_2 NRs is highly stepped. Atomic steps are frequently observed, as highlighted in red circles in Figure 3e. Further, steps with multiple atomic layers are also observed (Figure S2b, Supporting Information). Overall, the {110} facet exposes the low-coordinate surface cerium cations in both terraces and step sites. CeO_2 NRs grow along the [110] direction and are enclosed by {110} and {100} facets, as the scheme shown in the inset of Figure 3a.

Figure 4a presents the XRD patterns of Au/CeO_2 nanocomposites, formed by depositing Au NPs on CeO_2 NRs. No diffraction patterns from Au are observed in Au/CeO_2, indicating that Au NPs are small in size and finely dispersed on CeO_2 surface. Both 7.3 wt % Au/CeO_2 and 11.6 wt % Au/CeO_2 show blue shifts in the bands of 2TA (250 cm^{-1}), oxygen vacancies (564 cm^{-1}), and F_{2g} (457 cm^{-1}) with respect to that of CeO_2 NRs in Raman spectra (Figure 4b).[26] Figure 4c shows high-resolution XPS spectra of the Ce 3d core level with curve-fitting. The concentration of near-surface Ce^{3+} is estimated to be ~20% for Au/CeO_2 nanocomposites. Figure 4d exhibits high resolution of Au 4f core-level spectra of Au/CeO_2 nanocomposites. The Au spectra are well fitted by three sets of doublets located at 84.0 (Au^0), 84.6 (Au^+), and 86.2 eV (Au^{3+}), respectively.[26] The detailed fitting parameters are displayed in Table S2 (Supporting Information). Apparently, metallic gold (Au^0) is the dominant species (80.3% and 87.0% for 7.3 wt % Au/CeO_2 and 11.6 wt % Au/CeO_2, respectively) that is visible-light-responsive via unique SPR effects. The O 1s core-level spectra are depicted in Figure S3 (Supporting Information).

Figure 5a displays DRUV−vis spectra that are converted from the corresponding diffused reflectance spectra data on the basis of the Kubelka−Munk function. A very small red shift is observed in CeO_2 NRs relative to NCs, suggesting that the quantum-size effect is excluded.[31] The band gap (E_g) is estimated with a Tauc plot (Figure 5b): CeO_2 NRs and NCs possess a band gap of 2.90 and 3.10 eV, respectively. As shown in the inset of Figure 5a, Au/CeO_2 nanocomposites display typical absorption in the visible region that is caused by SPR on gold NPs.[25] As for 7.3 wt % Au/CeO_2 and 11.6 wt % Au/CeO_2, the respective absorption maximum is located at about 540 and 554 nm. Further, the absorption intensity is increased ~8%, with Au loading increasing from 7.3 to 11.6 wt %. The increased photoabsorption from Au SPR is expected to enhance visible light harvest and promote the photocatalytic performance.

The morphologies and size distributions of Au NPs are displayed in Figure 6. The Au NPs are highly dispersed on

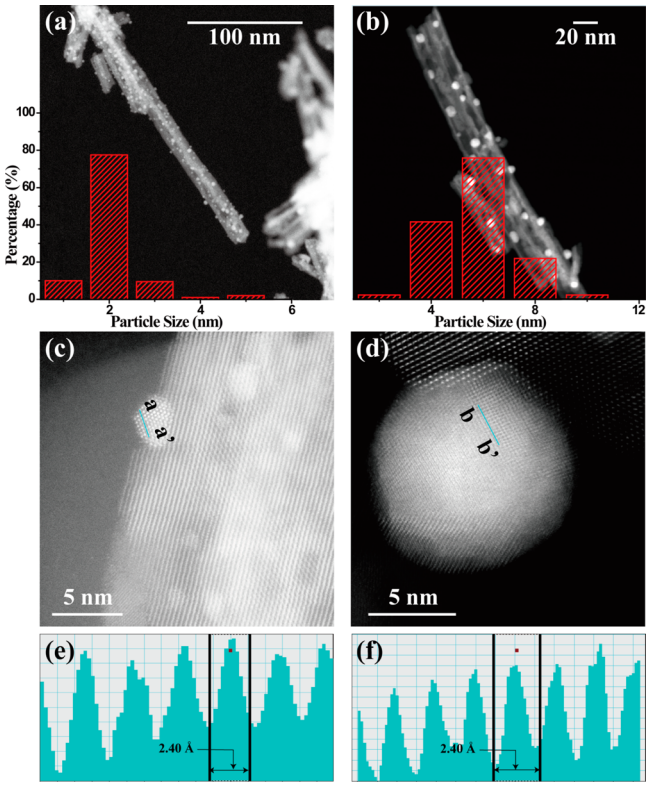

Figure 6. Low-magnification of HAADF-STEM images of (a) 7.3 wt % Au/CeO_2, (b) 11.6 wt % Au/CeO_2. Insets: the size distributions of Au NPs. High-magnification of HAADF-STEM images of Au NPs in (c) 7.3 wt % Au/CeO_2, (d) 11.6 wt % Au/CeO_2. Line profiles (e) along a−a′ in image c, and (f) along b−b′ in image d.

CeO_2 surface, as shown in Figure 6a and b. Statistical analysis of Au NPs from HAADF-STEM images reveals that the average size of gold NPs is 2.0 and 5.0 nm for 7.3 wt % Au/CeO_2 and 11.6 wt % Au/CeO_2, respectively. Faceted gold NPs are frequently observed, as shown in Figure 6c and d. The interatomic distance along both a−a′ and b−b′ (Figure 6e and f) is 2.40 Å, which is well ascribed to the metallic Au(111) plane.

DOI: 10.1021/acscatal.5b00620
ACS Catal. 2015, 5, 4385−4393

Photocatalytic Properties. The photocatalytic activity of the as-synthesized samples was evaluated toward MO photodegradation in water. To assess the photoreactivity of CeO_2 nanocrystals and Au/CeO_2 nanocomposites quantitatively, the reaction rate constants of MO degradation were calculated on the basis of the Langmuir−Hinshelwood kinetics. The photodegradation of aqueous MO is a pseudo-first-order reaction, and its kinetics could be expressed as $\ln(C/C_0) = -kt$, where k is the apparent reaction constant, C_0 is the initial absorbance of aqueous MO solutions, t is the reaction time, and C is the absorbance at t. Then k is determined by a linear regression method. For comparison, the blank test was conducted, and the photolysis was not observed under illumination (data not shown). With photocatalysts under the identical experimental conditions, the reaction rate is distinct between CeO_2 NRs and NCs. To explore the intrinsic photoactivity, k was normalized to the specific surface area, referred to k_s, which is 1.6×10^{-4} $min^{-1}{\cdot}L{\cdot}m^{-2}$ for CeO_2 NRs. In contrast, CeO_2 NCs show negligible activity. In general, reactant adsorption is a prerequisite step for heterogeneous photocatalysis.[9] The adsorption capacity of MO on CeO_2 NRs was estimated to be 62.8×10^{-3} $mmol{\cdot}g^{-1}$. In contrast, MO adsorption on CeO_2 NCs was negligible, as shown in Table S1 (Supporting Information).

To study the effects of loading Au NPs on the photocatalytic activity of CeO_2, CeO_2 NRs were selected as a support. Figure 7a and b display the reaction rate constants of Au/CeO_2 nanocomposites for MO photodegradation under UV and visible-light irradiation, respectively. The photoreactivity of Au/CeO_2 nanocomposites is enhanced significantly compared with CeO_2 NRs. For example, under UV, the reaction rate constants are 11.5×10^{-3} (2.0 nm Au NPs) and 16.6×10^{-3} min^{-1} (5.0 nm Au NPs) for Au/CeO_2 nanocomposites, greater than that of CeO_2 NRs by a factor of 2 and 3, respectively. Increasing the size of Au NPs from 2.0 to 5.0 nm improves the photoreactivity under both UV and visible light illumination. In the case of Au NPs with 5.0 nm in size, the reaction rate constant displayed by Au/CeO_2 nanocomposites under UV is $\sim 16.6 \times 10^{-3}$ min^{-1}, a little greater than that under visible light (12.4×10^{-3} min^{-1}). Additionally, the reaction rate constant of supported Au NPs with 5.0 nm size ($k = 12.4 \times 10^{-3}$ min^{-1}) displays 4 times larger than that with 2.0 nm ($k = 2.6 \times 10^{-3}$ min^{-1}) under visible light.

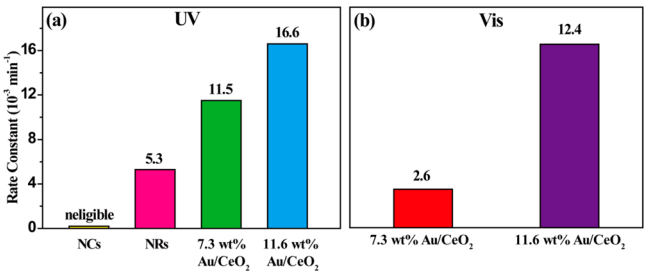

Figure 7. Photodegradation of MO in the presence of (a) CeO_2 photocatalysts under UV illumination. (b) Au/CeO_2 nanocomposites under visible light illumination. Reaction conditions: MO concentration 4×10^{-5} M, catalyst concentration 0.5 $g{\cdot}L^{-1}$, initial pH 6.3, 300 W Xe lamp (UV: 250−380 nm, light intensity is 300 $mW{\cdot}cm^{-2}$).

DISCUSSION

For a given photocatalyst, the photocatalytic performance is primarily determined by its electronic structure and surface structure.[13,23,32] The electronic structure of CeO_2 nanocrystals is revealed by DRUV−vis spectroscopy and high-resolution XPS, as mentioned above. Although CeO_2 NRs and NCs have comparable optical absorbance, the absorption edge of NRs displays a red shift (~12 nm) with respect to NCs. As a result, the band gap of NRs (2.90 eV) is relatively smaller than that of NCs (3.10 eV). Additionally, the line shape and width (6.01 eV) of VB are identical (Figure S1, Supporting Information) between CeO_2 NRs and NCs. On the other hand, the VB maximums of NCs and NRs are located at 1.96 and 2.28 eV, respectively. Thus, the respective conduction band minimums (CBM) of NCs and NRs are at 1.14 and 0.62 eV.

Generally, the redox ability of photocatalyst is determined by its band structure.[13] Nevertheless, CeO_2 NCs exhibit negligible photoreactivity. Therefore, it is reasonable to conclude that electronic structure does not play a leading role in determining the photocatalytic activity of CeO_2 NRs and NCs. It is well-known that the {100} facet of CeO_2 is an inherent polar surface, and the resulting polarization could be compensated by structural reconstructions. In a simplified viewpoint, half of the outermost oxygen anions are removed.[20]

Currently, the exact surface crystallographic terminations of nanoscaled CeO_2 are still under debate. Pan et al. reported two surface reconstructions, including (2×2) and (2×2) on CeO_2 (100) thin films by scanning tunneling microscopy (STM).[33] Previous studies[8,34] have reported the exposed facets of truncated CeO_2 NCs and NRs; however, no detailed surface atomic arrangements were examined because of the difficulty of detecting oxygen anions in HAADF-STEM imaging. Using aberration-corrected high-resolution electron microscopy (HREM), Lin et al.[20] examined the surface structures of CeO_2 nanocrystals and found that the {100} facet has complex terminations including Ce, O, and reduced CeO, which are different from our ABF-STEM imaging results owing to different synthesis approaches. Keep in mind that the surface structures of catalyst particles are often synthesis-dependent.[35]

In the present study, for the first time, our ABF-STEM imaging results demonstrate that the exposed {100} facet at CeO_2 NCs is nearly O-terminated without relaxations and reconstructions. On the basis of the current results, we propose the following mechanisms: First, near-surface oxygen vacancies, as evidenced by Raman and high-resolution XPS spectra, can offer positive charge and primarily compensate the polarity. Second, the cutoff facets at the corners and edges are in part responsible for stabilizing the {100} polar surface. The resulting O-terminated surface is negatively charged. The poor dye adsorption capacity of NCs stems from the repulsive interaction between the anionic MO dye and the negatively charged {100} facet.[32] In contrast, the surface structure of the {110} facet presents a mix of Ce cations and O anions in terraces, in addition to atomic steps. The low-coordinate unsaturated surface cerium cations on terraces and steps in turn act as MO adsorption and subsequent reaction sites. We conclude that the photoreactivity of CeO_2 nanocrystals is strongly surface-structure-sensitive, in the order {110} ≫ {100}. The underlying surface-structure sensitivity can be attributed to the variation in low-coordinate surface cerium cations between {110} and {100} facets. Further, the stability of {100} and {110} facets after being used for three cycles of MO

DOI: 10.1021/acscatal.5b00620
ACS Catal. 2015, 5, 4385−4393

Scheme 1. Proposed Mechanisms for MO Degradation by (a) CeO_2 Nanocrystals under UV Light and (b) (left) Au/CeO_2 Nanocomposites under UV Illumination and (right) under Visible Light Excitation

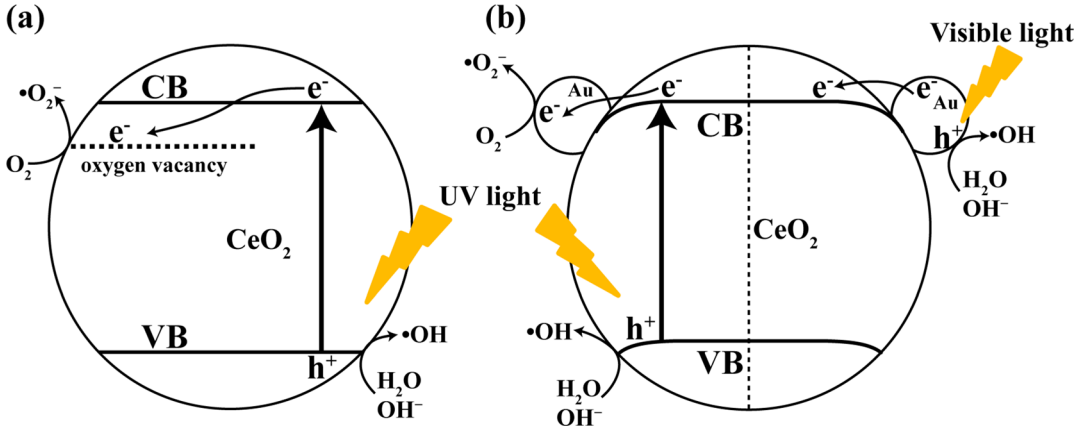

photodegradation are investigated, and the results are presented in Figure S4 (Supporting Information). The outermost surface layer of the {100} facets after reaction is still O-terminated, and significant reconstruction is not visualized in Figure S4a. Figure S4b also shows that the atomic surface structure of {110} facet is well-ordered after reactions. The above results demonstrate that the {100} and {110} facets are pretty stable against photocorrosion.

The mechanisms for the photodegradation of MO on CeO_2 nanocrystals and Au/CeO_2 plasmonic nanocomposites are proposed in Scheme 1. Scheme 1a shows the photocatalytic mechanism of CeO_2 under UV light irradiation. First, electrons are excited from VB to CB of CeO_2 and electron−hole pairs are formed. The resulting holes react with H_2O or OH^- to generate hydroxyl radicals (•OH), and the electrons could be trapped by oxygen vacancies near the surface of CeO_2 and then captured by oxygen molecules adsorbed at the oxygen-deficient Ce (III) sites to generate Ce-coordinated superoxide species Ce(IV)−O−O•.[36] Then $•O_2^-$ reacts with H^+ to form other active species, such as HO_2• or •OH radicals.[10] The high oxidative species are responsible for the mineralization of MO. The surface coordinated unsaturated cerium cations are the adsorption centers for MO dyes.[7]

As for photocatalysis driven by supported Au NPs under light illumination, there exist a number of possible mechanisms.[12,37,38] As an n-type semiconductor, the Fermi energy of CeO_2 is located at an energy level slightly lower than its CB. The Fermi energy of Au NPs is higher than that of CeO_2. When Au NPs and CeO_2 are in contact, the energy bands of CeO_2 bend downward toward the interface to reach an equilibrium as shown in Scheme 1b.[39] Upon visible light illumination, Au electrons are excited from 6sp to higher energy states via intraband transitions.[10] The electrons from Au NPs are injected rapidly into the CB of CeO_2, as shown in the right panel of Scheme 1b. Those electrons are trapped by near-surface oxygen vacancies adjacent to the interface of Au/CeO_2,[12] and then trigger the photooxidation reaction. Upon UV light excitation, the photogenerated electrons in CeO_2 are transferred to Au NPs quickly prior to being trapped by oxygen vacancies and, together with holes, initiate the photocatalytic reaction (the left panel of Scheme 1b).[12] In this case, Au NPs serve as electron trap centers and promote the charge separation to some extent. In addition, interband transitions from 5d to 6sp occur on Au NPs, leaving holes in the relatively lower energy 5d band but with higher oxidation capacity than those in the 6sp induced by visible light. Accordingly, greater photoreactivity under UV is achieved in comparison to visible light.

CONCLUSIONS

By virtue of advanced aberration-corrected STEM, we directly identified both oxygen and cerium on CeO_2 NCs and NRs. CeO_2 NCs predominantly expose the {100} facet, with minor {110} and {111} cutoff facets at the respective edges and corners. Additionally, the outermost surface layer of the {100} facet is oxygen-terminated without relaxations and reconstructions, indicating that near-surface oxygen vacancies are primarily responsible for polarity compensation. In contrast, the surface of CeO_2 NRs is highly stepped, and the {110} facet exposes Ce cations and O anions on atomic terraces. On the basis of STEM profile-view imaging and electronic structure analysis, UV light induced aqueous MO degradation on ceria nanocrystals is revealed to be surface structure sensitive, following the order {110} ≫ {100}. The underlying surface-structure sensitivity of CeO_2 nanocrystals in photocatalysis highlights the indispensable role of low-coordinate surface cerium cations in photocatalysis.

Loading Au NPs onto CeO_2 NRs to form Au/CeO_2 plasmonic nanocomposites dramatically enhances aqueous MO photodegradation, which is found to be Au particle size- and excitation light wavelength-dependent. In the case of 11.6 wt % Au/CeO_2, the photoreactivity under UV light is increased by 1.3 times than that of visible light. Under visible light illumination, upon increasing the Au particle size from 2.0 to 5.0 nm, the reaction rate constant is increased by a factor of ∼4. This study not only provides a new atomic-level understanding of structure−photoreactivity relationships in ceria photocatalysts, but also has broad implications in ceria-based water-splitting, among others.

ASSOCIATED CONTENT

Supporting Information

The Supporting Information is available free of charge on the ACS Publications website at DOI: 10.1021/acscatal.5b00620.

Valence band spectra and XPS spectra of O 1s core-level of CeO_2 samples. ABF-STEM and HAADF-STEM images of CeO_2 nanocrystals (PDF)

DOI: 10.1021/acscatal.5b00620
ACS Catal. 2015, 5, 4385−4393

AUTHOR INFORMATION

Corresponding Authors

*E-mail: liug@nanoctr.cn.
*E-mail: liuminghua@nanoctr.cn.

Notes

The authors declare no competing financial interest.

ACKNOWLEDGMENTS

We gratefully acknowledge the financial support of this work from National Natural Science Foundation of China (51272048).

REFERENCES

(1) Liyanage, A. D.; Perera, S. D.; Tan, K.; Chabal, Y.; Balkus, K. J., Jr. *ACS Catal.* **2014**, *4*, 577−584.
(2) Zhang, T. T.; Lei, W. Y.; Liu, P.; Rodriguez, J. A.; Yu, J. G.; Qi, Y.; Liu, G.; Liu, M. H. *Chem. Sci.* **2015**, DOI: 10.1039/c5sc00766f.
(3) Tanaka, A.; Hashimoto, K.; Kominami, H. *J. Am. Chem. Soc.* **2012**, *134*, 14526−14533.
(4) Zhang, T. T.; Zhao, K.; Yu, J. G.; Jin, J.; Qi, Y.; Li, H. Q.; Hou, X. J.; Liu, G. *Nanoscale* **2013**, *5*, 8375−8383.
(5) Ran, J. R.; Zhang, J.; Yu, J. G.; Jaroniec, M.; Qiao, S. Z. *Chem. Soc. Rev.* **2014**, *43*, 7787−7812.
(6) Campbell, C. T. *Top. Catal.* **2013**, *56*, 1273−1276.
(7) Zhou, X. M.; Lan, J. Y.; Liu, G.; Deng, K.; Yang, Y. L.; Nie, G. J.; Yu, J. G.; Zhi, L. J. *Angew. Chem., Int. Ed.* **2012**, *51*, 178−182.
(8) Agarwal, S.; Lefferts, L.; Mojet, B. L.; Ligthart, D. A. J. M.; Hensen, E. J. M.; Mitchell, D. R. G.; Erasmus, W. J.; Anderson, B. G.; Olivier, E. J.; Neethling, J. H.; Datye, A. K. *ChemSusChem* **2013**, *6*, 1898−1906.
(9) Zhou, X. M.; Xu, Q. L.; Lei, W. Y.; Zhang, T. T.; Qi, X. Y.; Liu, G.; Deng, K.; Yu, J. G. *Small* **2014**, *10*, 674−679.
(10) Lan, J. Y.; Zhou, X. M.; Liu, G.; Yu, J. G.; Zhang, J. C.; Zhi, L. J.; Nie, G. J. *Nanoscale* **2011**, *3*, 5161−5167.
(11) Li, Y.; Shen, W. J. *Chem. Soc. Rev.* **2014**, *43*, 1543−1574.
(12) Priebe, J. B.; Karnahl, M.; Junge, H.; Beller, M.; Hollmann, D.; Brückner, A. *Angew. Chem., Int. Ed.* **2013**, *52*, 11420−11424.
(13) Pan, J.; Liu, G.; Lu, G. Q.; Cheng, H. M. *Angew. Chem., Int. Ed.* **2011**, *50*, 2133−2137.
(14) Liu, J. W.; Lu, R. T.; Xu, G. W.; Wu, J.; Thapa, P.; Moore, D. *Adv. Funct. Mater.* **2013**, *23*, 4941−4948.
(15) Sun, C. W.; Li, H.; Chen, L. Q. *Energy Environ. Sci.* **2012**, *5*, 8475−8505.
(16) Paier, J.; Penschke, C.; Sauer, J. *Chem. Rev.* **2013**, *113*, 3949−3985.
(17) Melchionna, M.; Fornasiero, P. *Mater. Today* **2014**, *17*, 349−357.
(18) Mann, A. K. P.; Wu, Z. L.; Calaza, F. C.; Overbury, S. H. *ACS Catal.* **2014**, *4*, 2437−2448.
(19) Si, R.; Flytzani-Stephanopoulos, M. *Angew. Chem.* **2008**, *120*, 2926−2929.
(20) Lin, Y. Y.; Wu, Z. L.; Wen, J. G.; Poeppelmeier, K. R.; Marks, L. D. *Nano Lett.* **2014**, *14*, 191−196.
(21) Primo, A.; Marino, T.; Corma, A.; Molinari, R.; García, H. *J. Am. Chem. Soc.* **2011**, *133*, 6930−6933.
(22) Urban, K. W. *Science* **2008**, *321*, 506−510.
(23) Tong, H.; Ouyang, S. X.; Bi, Y. P.; Umezawa, N.; Oshikiri, M.; Ye, J. H. *Adv. Mater.* **2012**, *24*, 229−251.
(24) Rodriguez, J. A.; Ramírez, P. J.; Asara, G. G.; Viñes, F.; Evans, J.; Liu, P.; Ricart, J. M.; Illas, F. *Angew. Chem.* **2014**, *126*, 11452 −11456.
(25) Kominami, H.; Tanaka, A.; Hashimoto, K. *Chem. Commun.* **2010**, *46*, 1287−1289.
(26) Xu, Q. L.; Lei, W. Y.; Li, X. Y.; Qi, X. Y.; Yu, J. G.; Liu, G.; Wang, J. L.; Zhang, P. Y. *Environ. Sci. Technol.* **2014**, *48*, 9702−9708.
(27) Fabris, S.; Vicario, G.; Balducci, G.; Gironcoli, S. de; Baroni, S. *J. Phys. Chem. B* **2005**, *109*, 22860−22867.
(28) Liu, G.; Rodriguez, J. A.; Hrbek, J.; Dvorak, J.; Peden, C. H. F. *J. Phys. Chem. B* **2001**, *105*, 7762−7770.
(29) Xu, Z. T.; Jin, K. J.; Gu, L.; Jin, Y. L.; Ge, C.; Wang, C.; Guo, H. Z.; Lu, H. B.; Zhao, R. Q.; Yang, G. Z. *Small* **2012**, *8*, 1279−1284.
(30) Hojo, H.; Mizoguchi, T.; Ohta, H.; Findlay, S. D.; Shibata, N.; Yamamoto, T.; Ikuhara, Y. *Nano Lett.* **2010**, *10*, 4668−4672.
(31) Sun, C. W.; Li, H.; Zhang, H. R.; Wang, Z. X.; Chen, L. Q. *Nanotechnology* **2005**, *16*, 1454−1463.
(32) Jiang, J.; Zhao, K.; Xiao, X. Y.; Zhang, L. Z. *J. Am. Chem. Soc.* **2012**, *134*, 4473−4476.
(33) Pan, Y.; Nilius, N.; Stiehler, C.; Freund, H.-J.; Goniakowski, J.; Noguera, C. *Adv. Mater. Interfaces* **2014**, *1*, DOI: 10.1002/admi.201400404.
(34) Cordeiro, M. A. L.; Weng, W. H.; Stroppa, D. G.; Kiely, C. J.; Leite, E. R. *Chem. Mater.* **2013**, *25*, 2028−2034.
(35) Lin, Y. Y.; Wen, J. G.; Hu, L. H.; Kennedy, R. M.; Stair, P. C.; Poeppelmeier, K. R.; Marks, L. D. *Phys. Rev. Lett.* **2013**, *111*, 156101−1−156101−5.
(36) Li, B. X.; Gu, T.; Ming, T.; Wang, J. X.; Wang, P.; Wang, J. F.; Yu, J. C. *ACS Nano* **2014**, *8*, 8152−8162.
(37) Zhou, X. M.; Liu, G.; Yu, J. G.; Fan, W. H. *J. Mater. Chem.* **2012**, *22*, 21337−21354.
(38) Chen, X.; Zheng, Z. F.; Ke, X. B.; Jaatinen, E.; Xie, T. F.; Wang, D. J.; Guo, C.; Zhao, J. C.; Zhu, H. Y. *Green Chem.* **2010**, *12*, 414−419.
(39) Zhang, Z.; Yates, J. T., Jr. *Chem. Rev.* **2012**, *112*, 5520−5551.

DOI: 10.1021/acscatal.5b00620
ACS Catal. 2015, 5, 4385−4393